Journal of Alloys and Compounds 851 (2021) 156330

Contents lists available at ScienceDirect

Journal of Alloys and Compounds

journal homepage: http://www.elsevier.com/locate/jalcom

Fe–Co coatings electrodeposited from eutectic mixture of choline chloride-urea: Physical characterizations and evaluation as electrocatalysts for the hydrogen evolution reaction

Francisco G.S. Oliveira [a, *], F. Bohn [b], Adriana N. Correia [c], Igor F. Vasconcelos [d], Pedro de Lima-Neto [c]

[a] Pós-Graduação em Engenharia e Ciências de Materiais, Centro de Tecnologia, Universidade Federal do Ceará, Campus do Pici, Bloco 729, 60440-900, Fortaleza, CE, Brazil
[b] Departamento de Física, Universidade Federal do Rio Grande do Norte, 59078-970, Natal, RN, Brazil
[c] Departamento de Química Analítica e Físico-Química, Centro de Ciências, Universidade Federal do Ceará, Campus do Pici, Bloco 940, 60440-900, Fortaleza, CE, Brazil
[d] Departamento de Engenharia Metalúrgica e de Materiais, Centro de Tecnologia, Universidade Federal do Ceará, Campus do Pici, Bloco 729, 60440-900, Fortaleza, CE, Brazil

ARTICLE INFO

Article history:
Received 14 April 2020
Received in revised form
24 June 2020
Accepted 6 July 2020
Available online 18 August 2020

Keywords:
Electrodeposition of Fe–Co coatings
Deep Eutectic Solvent
Magnetic properties
Mössbauer spectroscopy
Hydrogen evolution reaction

ABSTRACT

Fe–Co coatings were electrodeposited on Cu substrates from a choline chloride-urea eutectic solution. The influence of Fe and Co content on the magnetic, morphological, and electrocatalytic properties of the electrodeposits was duly studied. The coercivity and quadrature of the magnetic hysteresis curves revealed that all coatings had soft magnetic properties that varied with the coating composition. A hyperfine magnetic field between 36 and 38 T in their Mössbauer spectra indicated the formation of Fe–Co alloy in the samples $Fe_{87}Co_{13}$, $Fe_{64}Co_{36}$, and $Fe_{44}Co_{56}$. All coatings with Fe content higher than 25% showed magnetic texture along their growth axis with orientation angles ranging from $\theta = 5.1$ to 42.8°. The Fe, Co, and Fe–Co coatings showed good electrocatalytic performance for the hydrogen evolution reaction, with mainly the Fe-rich coatings presenting the lowest values of overpotential. Remarkably, an Fe coating afforded a current density of 10 cm^{-1} at a low overpotential of 89.2 mV, as well as exhibiting a small Tafel slope of 44.6 mV dec^{-1} in 0.5 mol L^{-1} NaOH. The results showed that the use of choline chloride-urea eutectic solution provides a promising and ecological strategy for the production of Fe–Co coatings since it is not necessary to add other chemicals besides the corresponding metallic salts.

1. Introduction

The study of the magnetic properties in ferromagnetic coatings is always an important aspect of these materials and determines their possible applications. In addition, materials with soft magnetic properties have been gaining a lot of attention because they have interesting characteristics, for instance, high saturation magnetization as well as low coercivity. Such properties are essential in several technological applications such as magnetic recording heads [1,2], spin-based electronic devices [3,4], and miniaturization of devices [5]. Among these materials, the Fe–Co alloys stand out for having important properties such as high Curie temperature, high permeability, low hysteresis loss, excellent thermal stability [6–8], and high anisotropy energy [9,10]. All these characteristics allow the Fe–Co coatings to have a wide variety of technological applications that cover different areas of knowledge, for instance, microwave absorption [11], high-density data storage [12], magnetic resonance imaging [13], micro-inductors [14,15], drug delivery [16], and electrocatalysis [17].

The production of hydrogen fuel from water electrolysis has become an excellent alternative to produce clean and renewable energy with a low environmental impact [18–21]. The electrocatalysis of the Hydrogen Evolution Reaction (HER) is linked to the use of Pt, Ag, and Au based electrocatalysts materials since they are the most efficient materials for the HER [22]. However, these noble metals are scarcity on the terrestrial coast and, consequently, they are awfully expensive, which limits their large-scale use [23,24]. In

* Corresponding author.
E-mail address: gilvane@alu.ufc.br (F.G.S. Oliveira).

https://doi.org/10.1016/j.jallcom.2020.156330
0925-8388/

this context, the study and application of new materials that present a good electrocatalytic response and which are not expensive, as well as being abundant, have stood out. Among the most promising materials listed are the binary alloys prepared by the combination of the following metals: Fe, Co, Ni, and Mo [17,25–31].

Fe–Co coatings are usually produced using high vacuum and high-temperature techniques, such as the physical gas condensation system [32], thermal decomposition [33], pulsed laser deposition [34], and sputtering [35], amongst others. Nevertheless, all these techniques require high precision of process control, making the large-scale production expensive. On the other hand, chemical methods have been used to prepare highly effective and low-cost Fe–Co compounds. Hao et al. [17] reported the synthesis of binary transition metal phosphide ($Co_xFe_{1-x}P$) nanocubes with different Co and Fe ratios through a phosphating process using metal-organic frameworks (MOFs) as templates. The authors claimed that the material $Co_{59}Fe_{41}$ prepared at 450°C delivered the best HER kinetics in both acidic and alkaline conditions, showing a low overpotential (72 mV) in 10 mA cm^{-2}, small Tafel slope (52 mv dec^{-1}), and high exchange current density (0.517 mA^{-2}). Moreover, Yuan et al. [31], obtained ferrite MFe_2O_4 (M = Fe, Co, Ni) tubular microstructures by a simple two-step strategy, where the tubular FeOOH microstructures were first obtained by a heating reflux route and a solvothermal method was utilized to prepare tubular MFe_2O_4 microstructures. According to this study, the ferrite $NiFe_2O_4$ showed the best electrocatalytic activities for HER and OER due to the largest specific surface area, the highest electrochemically active surface area, and the smallest charge transfer resistance. However, these synthetic route approaches involve more than a one-step process, long reaction times, and high temperatures. In contrast, Lu et al. [36], reported the successful electrodeposition of Fe–Co films on a Cu substrate in acid-based electrolytes. Therefore, the electrodeposition technique is an attractive alternative method to produce Fe–Co electrodeposited coatings, since it is easy to use and of low cost, making it suitable for applications on an industrial scale [37,38]. This technique allows the control of the thickness and composition of the coating and it can be deposited on the substrate's surface in different geometries. Furthermore, in comparison with the vacuum deposition techniques, electrodeposition makes it possible to improve the magnetic properties since the improvements are related to a better organization and structural homogeneity of the films [25,39,40].

Traditionally, the electrodeposition of metals and alloys is carried out in aqueous-based electroplating solutions. However, the electrodeposition of individual metals and alloys requires the use of organic and inorganic additives, such as cyanide, that lead to the production of non-environmentally friendly wastewater [41]. Besides, for water plating solutions, Fe and Co are metals that are electrodeposited in the potential range of the HER, which decreases the cathodic current efficiency and can affect the coating's adherence, as well as producing gas bubbles which can be trapped in the electrodeposited layer. Furthermore, for Fe electrodeposition, it is recommended that the pH of the electroplating solutions be equal to, or less than 3.5, to minimize the precipitation of iron hydroxide ($Fe(OH)_3$) [42] since the $Fe(OH)_3$ precipitation hinders the kinetics of deposition and the magnetic properties of the Fe-based electrodeposited coatings [40,43]. However, electrodeposition carried out at a low pH range results in low cathodic efficiency and increases the stress of the electrodeposited layer [42].

Since 2007, electroplating solutions formulated from Deep Eutectic Solvents (DES) have been investigated as an environmentally friendly alternative to water-based electroplating solutions for the electrodeposition of individual metals and alloys [44]. The DESs are composed of quaternary ammonium salts mixed with a hydrogen bond donor [45,46]. These solvents offer new possibilities for the electrodeposition of materials. Notably, they are easy to prepare, do not react with water, have good ionic conductivity, have high thermal stability, and have good solubility in metallic salts [47,48]. Differently from the aqueous-based electroplating solutions, DES have managed to solve several electrodeposition problems such as toxicity of the complexing agent, a narrow electrochemical window, and the coating's embrittlement due to hydrogen caused by water electrolysis reactions [47,48]. All these characteristics are essential for the electrodeposition of metals and alloys [47]. Li et al. [49] studied the electrodeposition of Co at several cathodic potentials and different temperatures in a DES-based on choline chloride (ChCl) and urea (U), at a molar ratio of 1:2 (1ChCl:2U). The authors found that uniform, dense, and compact deposits were deposited at the most positive cathodic potential and lower temperatures. However, non-uniform, dendritic, and cauliflower-like structures of different sized deposits were formed at more negative cathodic potentials and higher temperatures. Furthermore, Yanai et al. [50] demonstrated that magnetic Fe–Co films can be successfully electrodeposited in a mixture of ChCl and ethylene glycol (EG) at a weight-mass of 1:1. These authors showed that the saturation magnetization and the coercivity of the films were influenced by the Fe content. Furthermore, the $Fe_{76}Co_{24}$ sample displayed high saturation magnetization and a smooth surface. However, no information about the structural and local chemical environment of the Fe sites characterization was found in the study. Sides et al. [25] carried out an extensive investigation on the electrodeposition of Fe, Co, Fe–Co, and Fe–Co–Mn alloys in a eutectic mixture of 1ChCl:2U. The authors claimed that the electrodeposition potentials of Fe and Co were close to each other, leading to easy alloy co-deposition, and enabling easy control of the deposit composition with the solution concentration. Also, Mn has been incorporated by an underpotential deposition mechanism to form tertiary Fe–Co–Mn alloys. However, the magnetization was lower than generally expected for pure bulk Fe–Co or Fe–Co–Mn alloys, likely due to impurities and cracks in the film. As presented above, the electrodeposition of Fe–Co films in DES has been investigated, however, the electrocatalytic properties of these coatings have not been investigated yet. Thus, this study aimed to investigate the electrodeposition of Fe, Co, and Fe–Co coatings on Cu substrate in the ratio 1ChCl:2U, using several chemical bath compositions, without additives, at the temperature of 353 K, and to characterize the magnetic properties of the electrodeposited coatings, as well to evaluate their electrocatalytic performance for HER in alkaline medium.

2. Materials and methods

2.1. Electrolyte preparation

The Fe, Co, and Fe–Co coatings were electrodeposited from a eutectic mixture of choline chloride (ChCl) ($HOC_2H_4N(CH_3)_3Cl$, Sigma-Aldrich, ≥ 98%) and urea (U) ($(NH_2)_2CO$, Sigma-Aldrich, ≥ 99%), used as received. The eutectic mixtures were prepared following the methodology described by Abbott et al., [46]. With a molar ratio of 1:2, these chemicals were mixed and heated to 353 K until the formation of a homogeneous and colorless liquid phase was reached. Immediately, after the DES cooling, the precursor metal salts, iron chloride ($FeCl_2$, Sigma-Aldrich ≥ 99%) and cobalt chloride ($CoCl_2$, Sigma-Aldrich ≥ 99%), were added under magnetic stirring. Table 1 presents the composition of the solutions used for the electrodeposition of the Fe–Co coatings.

2.2. Electrodeposition of Fe, Co, and Fe–Co coatings

All electrochemical experiments were performed in three-

Table 1
The composition obtained by EDS of Fe, Co, and FeCo coatings, electrodeposited in the different concentration electroplating solutions.

Bath composition		Coatings composition by EDS		Sample label	E_{peak}/ V
$FeCl_2$/ mol L^{-1}	$CoCl_2$/ mol L^{-1}	Fe (at%)	Co (at%)		
0.5	–	100	0	Fe	1.00
0.45	0.05	87 ±1.4	13 ±1.4	$Fe_{87}Co_{13}$	0.95
0.35	0.15	64 ±1.7	36 ±1.7	$Fe_{64}Co_{36}$	0.88
0.25	0.25	44 ±2.1	56 ±2.1	$Fe_{44}Co_{56}$	0.93
0.15	0.35	25 ±1.9	75 ±1.9	$Fe_{25}Co_{75}$	0.90
0.05	0.45	7 ±1.8	93 ±1.8	Fe_7Co_{93}	0.85
–	0.5	0	100	Co	0.90

electrode electrochemical cells at 353 K. The potentiostat/galvanostat (AUTO LAB PGSTAT30, Metrohm-Eco Chemie) was controlled by the NOVA software, version 2.11. The pseudo-reference was Ag/AgCl immersed in the eutectic mixture (1ChCl:2U), whereas the counter electrode was a Pt plate (≈ 2 cm^2). For the cyclic voltammetry measurements, the working electrode was a Cu disc with ≈ 0.18 cm in diameter. For physical characterization, the Fe, Co, and Fe–Co coatings were electrodeposited on a Cu tape (1 cm^2 of area and thickness of 20 μm), supported on a glass plate. For the electrocatalysis experiments, the Fe, Co, and Fe–Co coatings were electrodeposited on a Cu cylinder in epoxy resin and a disk area af about 2.04 cm^2. Before the electrodeposition, all electrodes underwent a cleaning process which included being degreased in a 10% NaOH solution, rinsing in Mili-Q water (18.2 MΩ• cm), immersion in 10% HCl solution and rinsed again in Mili-Q water. The Fe, Co, and Fe–Co coatings were electrodeposited under a potentiostatic control at the peak potentials duly identified in the cyclic voltammograms (Fig. 1a–f). The electrodeposition time was 30 min for all the working conditions. After the electrodeposition process, all coatings were washed with Mili-Q water to remove any excess solvent and then washed with isopropyl alcohol to completely remove the water from the surface. Thereafter, the coatings were air-dried. All the cyclic voltammograms were obtained at 353 K using the scan rate of 10 mV s^{-1} with the initial and final scan potential being −0.50 V relative to the pseudo-reference electrode Ag/AgCl, since the Cu oxidizes at applied potentials more positive than −0.4 V [51,52].

2.3. Physical and chemical characterization of the Fe–Co coatings

The morphological properties of Fe–Co coatings were investigated in a high-resolution scanning electron microscope (FEG-SEM, FEI-Quanta 450) operating at 20 kV. The chemical composition was determined by energy-dispersive X-ray spectroscopy (EDS) coupled to FEG-SEM. The compositional analysis was carried out for at least three samples. The X-ray diffraction (XRD) patterns of Fe, Co, and Fe–Co coatings were collected using a PANalytical diffractometer, model XPert PRO with Co-Kα (λ = 0.1788 nm) radiation working at 40 kV and 40 mA. The measurements were conducted in conventional Bragg-Brentano geometry.

The magnetic characterization of the Fe–Co coatings was obtained through magnetization curves at room temperature and the curves were acquired using a vibrating sample magnetometer (VSM) Lakeshore 7400 with a maximum magnetic field amplitude of 15 kOe. The VSM had been previously calibrated using a pure Ni sample, however, the normalized magnetization curves that give an accurate estimate of the coating mass were not obtained.

The Mössbaeur spectra were measured in a transmission mode using a $^{57}Co(Rh)$ radioactive source mounted on a velocity driver and operating in triangular mode. The data were evaluated by least-square fitting to a series of discrete Lorentzian shaped sub-spectra utilizing the software package NORMOS. The measured isomer shifts (δ) are fits concerning the α–Fe.

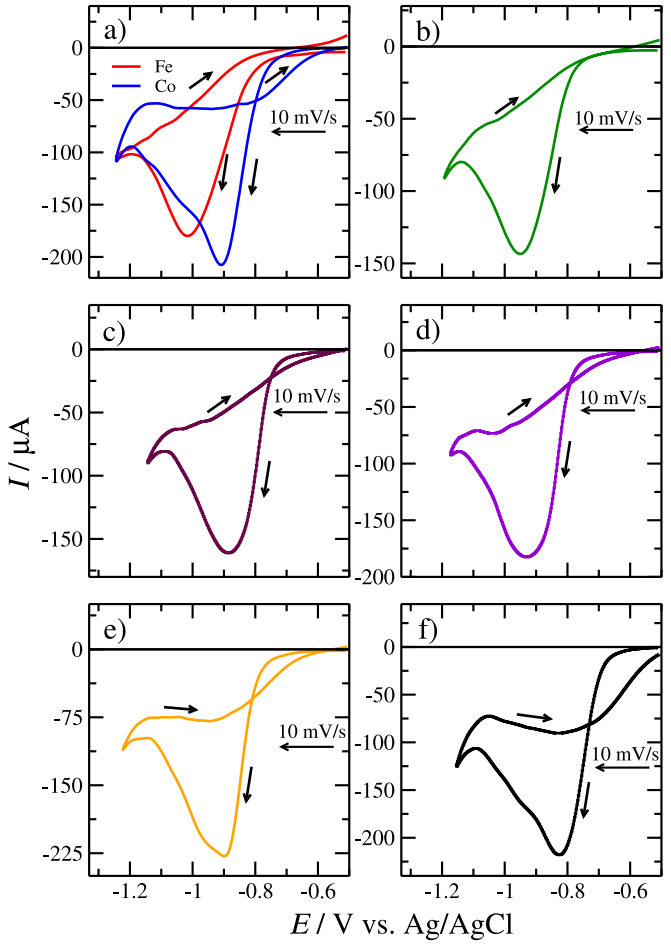

Fig. 1. Cyclic voltammograms obtained at different electroplaing solutions: (a) 0.5 mol L^{-1} $FeCl_2$ (Red Line) and 0.5 mol L^{-1} $CoCl_2$ (Blue Line), (b) 0.45 mol L^{-1} $FeCl_2$ + 0.05 mol L^{-1} $CoCl_2$, (c) 0.35 mol L^{-1} $FeCl_2$ + 0.15 mol L^{-1} $CoCl_2$, (d) 0.25 mol L^{-1} $FeCl_2$ + 0.25 mol L^{-1} $CoCl_2$, (e) 0.15 mol L^{-1} $FeCl_2$ + 0.35 mol L^{-1} $CoCl_2$, and (f) 0.05 mol L^{-1} $FeCl_2$ + 0.45 mol L^{-1} $CoCl_2$, in electroplating solutions. Scan rate 10 mV s^{-1}. (For interpretation of the references to color in this figure legend, the reader is referred to the Web version of this article.)

2.4. Electrocatalytic study of Fe–Co coatings for HER

The kinetic parameters of the Fe, Co, and Fe–Co coating for the HER were obtained by linear scanning voltammetry (LSV) at a scanning rate of 1 mV s^{-1}. The LSV curves were obtained in an alkaline solution 0.5 mol L^{-1} NaOH at 298 K. The used reference electrode was $Hg_{(s)}|HgO_{(s)}|OH^-$ (aq. 0.5 mol L^{-1}). However, the

measured potentials were converted to the reversible hydrogen electrode (RHE) scale using Equation (1), where $E_{vs.\ RHE}$ is the potential on the scale of RHE, and $E_{vs.\ Hg/HgO}$ is the potential on the scale of the $Hg_{(s)}|HgO_{(s)}|OH^-$ electrode. The long-range tests were performed in the continuous operating mode for 150 h, applying a current density of 50 mA cm^{-2} at 298 K.

$$E_{vs.RHE} = E_{vs.Hg/HgO} + 0.095 + 0.059pH \quad (1)$$

3. Results and discussion

3.1. Cyclic voltammetry

Typical cyclic voltammograms obtained for the electrochemical reduction of the individual species of the Fe^{2+}/Fe^0 and Co^{2+}/Co^0 on the copper surface are shown in Fig. 1a, while those achieved for both species dissolved in the electroplating solution are displayed in Fig. 1(b–f). It can be noted that each Fe^{2+} and for Co^{2+} species displayed only one cathodic peak, at −1.0 V and −0.9 V, respectively. For both Fe^{2+} and Co^{2+} dissolved in the same solution, Fig. 1(b–f) show that an overlap occurred at one peak potential (E_{peak}), varying between −0.82 and −0.95 V. All E_{peak} values are listed in Table 1.

3.2. Morphological, chemical composition and structural characterization of the coatings

The chemical composition of the coatings with the Fe^{2+} molar percentage in the plating solution is given in Fig. 2a, showing that the Fe percentage in the electrodeposited Fe–Co is always lower than the Fe^{2+} percentage in the corresponding plating solution. This particular behavior agrees with the study published by Lu et al. [36] for the electrodeposition of the Fe–Co coatings from an aqueous plating solution. Since the Co is a nobler metal than Fe, it is preferentially electrodeposited indicating that in the choline chloride-urea mixture, the electrodeposition of the Fe–Co coatings follows a normal electrodeposition.

The SEM images, displayed in Fig. 2b, show that all electrodeposited Fe, Co, and Fe–Co coatings are cracked and that the most cracked surfaces have the highest iron content. Again, this observation agrees with reports published by Lu et al. [36] and Sides et al. [25], which demonstrated that the Fe–Co coatings electrodeposited from aqueous solutions and choline chloride-urea, respectively, were cracked. The crack formation in metal electrodeposition is reported in several studies in the literature, especially in metal alloy electrodeposition. Lammel et al. [53] and Eliaz et al. [54] suggested that the occurrence of cracks is related to the high residual stress present in the coatings. The residual stress which gives rise to this type of morphology is derived from the substitution of larger atoms by smaller atoms in the crystalline structure of the alloy, or by the gas evolution during the electrodeposition process due to the water electrolysis [55,56]. The cracks may also be generated by interfacial mechanical coupling between the electrodeposited coating and the substrate, which is increased with the coating thickness or reduced with the grain size [57,58]. As in the choline chloride-urea mixture, the electrodeposition of Fe–Co does not occur simultaneously as the electrochemical reduction of the eutectic solvent, the cracks present in the Fe–Co electrodeposits being due to the internal tensions generated during the electrodeposition process. As the percentage of Co increases in the composition of the coatings, it can be seen that the morphologies undergo modifications making the coating surface less cracked when compared to the Fe electrodeposited coating, thus highlighting the spherical shapes that predominate in the Co electrodeposited coating.

In addition, XRD patterns from Fe, Co, and Fe–Co coatings are shown in Fig. 3 and reveal the peaks at 2θ at about 51° and 60°, assigned to the {111} and {200} set planes, respectively, which can be attributed the face-centered cubic (fcc) structure (space group Fm-3m [225]) from the Cu substrate, indexed with ICSD 52256. Moreover, the patterns exhibited peaks located at 2θ at around 49°, 52°, and 56°, corresponding to the set of crystallographic planes {100}, {002}, and {011} from the hexagonal phase of Co (space group P63/mmc [194]), which can be indexed with the ICSD 44990 data sheet. In contrast, no peaks from the Fe phase were detected in the patterns, probably due to the thin thickness of the coatings. On the other hand, the diffraction peak located at 2θ around 53° was attributed to the Fe–Co alloy, corresponding to the body-centered cubic (bcc) crystal structure (space group Im-3m [229]), according to the ICSD 102381 file card.

3.3. Magnetic properties

The magnetic properties of the Fe–Co electrodeposits were evaluated by magnetization curves acquired at room temperature and presented in Fig. 4. The analyses showed typical magnetic hysteresis loops of the Fe–Co coatings produced by the electrodeposition. In particular, it is possible to identify that the addition of the Co into the composition of the electrodeposits modifies the shape of the magnetization curves and also affects the values of the coercive field H_c, normalizing the remnant magnetization, i.e. the ratio between the remnant magnetization and the saturation magnetization that provides insights on the squareness of the curve. These values are shown in Table 2.

The highest values of the H_c were identified for $Fe_{87}Co_{13}$ and $Fe_{64}Co_{36}$ electrodeposits and they are indicators for the substitution of the Fe atoms by the Co atoms in the Fe bcc structure. This substitution process characterizes the formation of the Fe–Co alloy, inducing a significant number of defects in the crystal structure and as a result, changes the ordering of the magnetic domains and increases the hysteresis losses. This latter result is also directly related to the reduced normalized remnant magnetization values found for the aforementioned samples. However, with increasing Co content, a reduction of the coercivity and an increase of the squareness ratio are found, indicating that the coatings produced by the electroplating are materials of soft magnetic properties.

The relation between the coercive field and the concentration of the Co is shown in Fig. 5. The coercive field value in coatings increases with the addition of the Co and reaches a maximum value of 811 Oe in $Fe_{64}Co_{36}$. Therefore, there is a very sharp drop in the H_c with coatings with a higher concentration of Co, reaching 27 Oe at $Fe_{25}Co_{75}$. The change in the coercivity of the Fe–Co coatings is a result of microstructural variations caused by the increase in the Co concentration of the composition of the electrodeposits. According to Yiming et al. [59], the electrochemical reduction of the Fe^{2+} and Co^{2+} ions in temperatures superior to 323 K, happens quickly, therefore generating high internal tensions and several defects that lead to the appearance of slight distortions in the crystalline structure of the material [59]. When the Co is added to the bcc structure of the Fe, the hyperfine magnetic field increases [60,61]. Thus, the total magnetic moment increases followed by the coercive field Hc, which also increases with the addition of the Co. This particular behavior helps to understand the growth of the coercive field for $Fe_{87}Co_{13}$ and $Fe_{64}Co_{36}$ coatings, where the diffusion of the Co atoms in the Fe structure probably occurs and which characterizes the formation of the Fe–Co alloy in these aforementioned concentrations. However, for the other coatings, probably only a binary Fe and Co film is formed in separate structures. Presently, this interesting feature is not fully understood and is currently

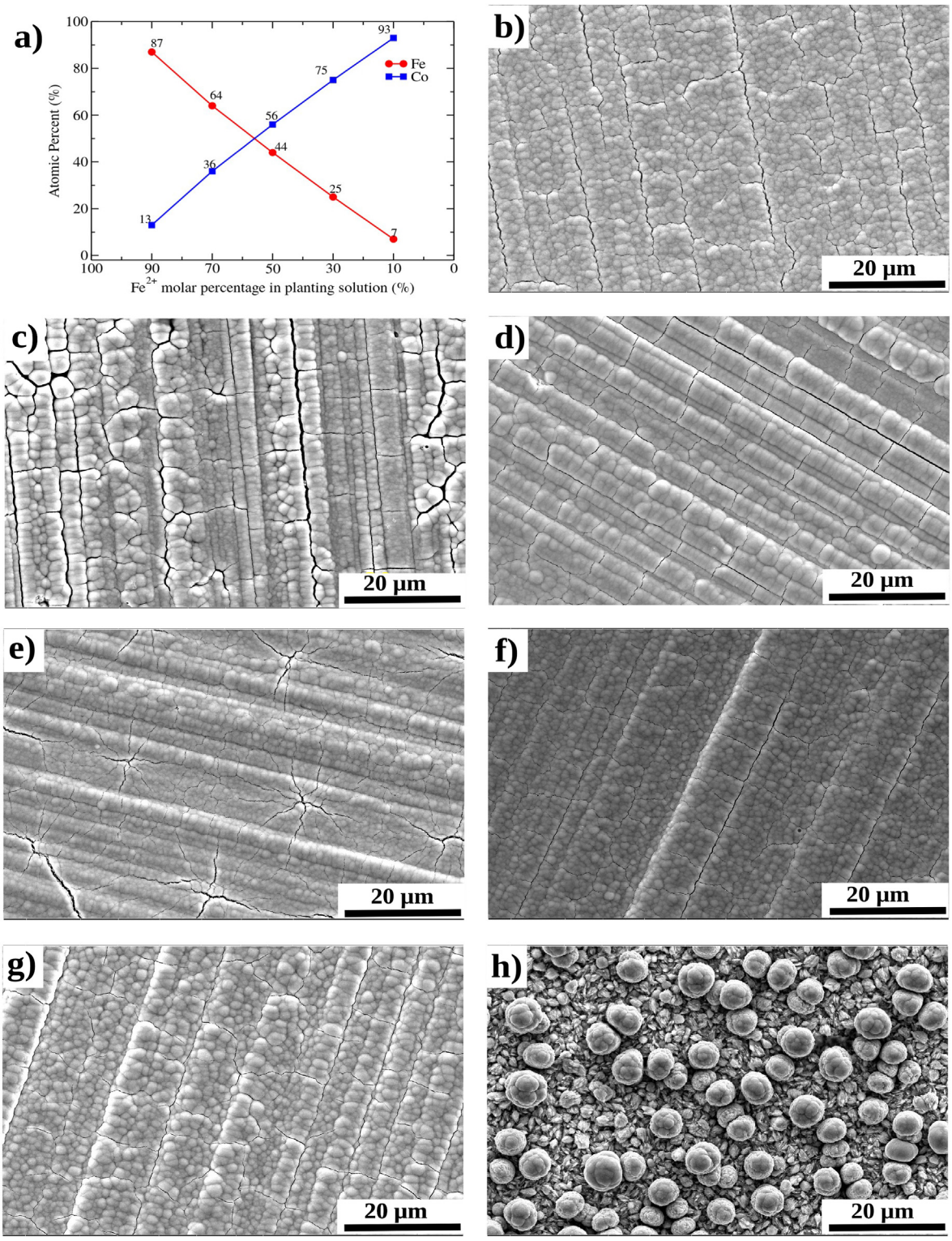

Fig. 2. (a) Plot showing atomic weigth percentece of Fe—Co coatings with the bath composition. SEM images obtained for electrodeposited Fe—Co: (b) Pure Fe, (c) $Fe_{87}Co_{13}$, (d) $Fe_{64}Co_{36}$, (e)$Fe_{44}Co_{56}$, (f) $Fe_{25}Co_{75}$, (g) $Fe_{7}Co_{93}$, and (h) Pure Co.

under investigation.

3.4. Mössbauer spectroscopy studies

Mössbauer spectroscopy is a useful technique to investigate iron sites and their chemical vicinities. Therefore, Mössbauer spectroscopy was used to confirm the formation of the Fe—Co phase, as well as obtain the parameters of the local magnetic texture, which is typical for thin ferromagnetic films [61]. Figs. 6 and 7 show the room temperature Mössbauer spectra of Fe, $Fe_{87}Co_{13}$, $Fe_{64}Co_{36}$, $Fe_{44}Co_{56}$, and $Fe_{25}Co_{75}$ coatings, along with the best fits to the data. The Fe coating is best fitted by the distribution

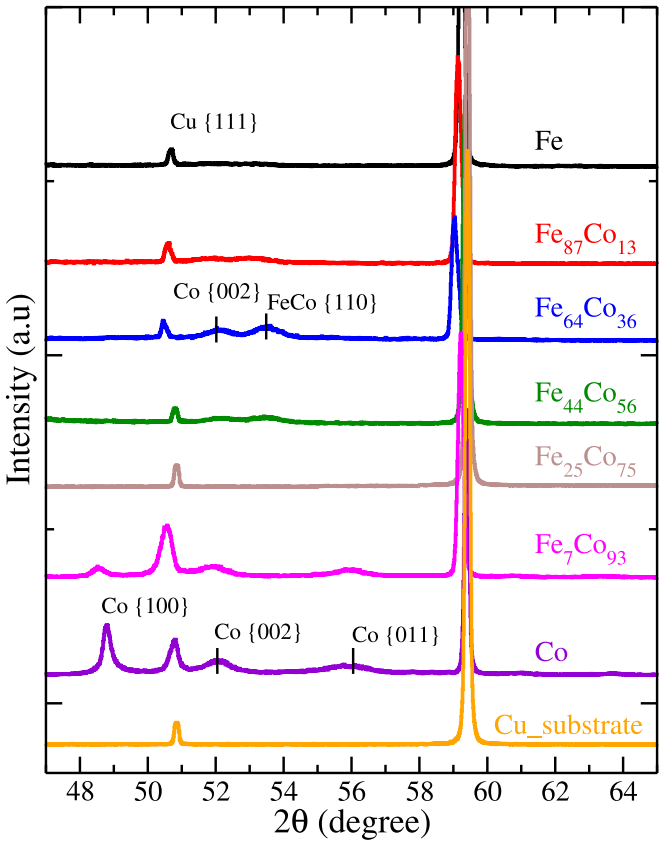

Fig. 3. XRD patterns of Fe, Co, and Fe–Co coatings electrodeposited at different in electroplating solutions.

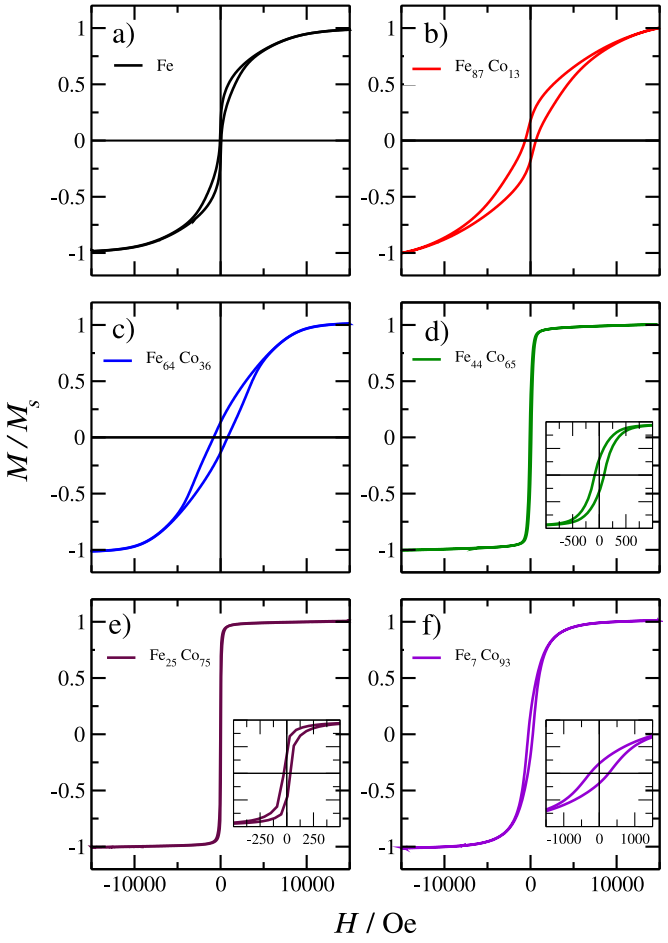

Fig. 4. Magnetization curves of the electrodeposited Fe–Co (a–f). Inset (d–f): magnification of curves for analysis of the magnetic hysteresis.

of the hyperfine magnetic field (B_{hf}), which reflects the randomness of the environment in which the Fe atoms are located [62]. With the addition of Co to the coatings, the Mössbauer spectra are fitted with two ferromagnetic sextets, indicating the dissolution of Co atoms in the bcc structure of Fe and the possible formation of a Fe-Co [63,64] magnetic alloy. The Fe_7Co_{93} coating did not present a sufficient absorption to enable a measurable spectrum because of the low Fe concentration.

Fig. 6 shows the Mössbauer spectrum of the Fe coating fitted with a ferromagnetic sextet distribution (green line) and two paramagnetic sites, represented by a singlet (violet line) and a doublet (orange line). The values of the hyperfine parameters are presented in Table 3. Fig. 6b shows the magnetic field distribution with a peak at $B_{hf} = 33$ T that is attributed to bcc α–Fe, and a region of low fields between 10 and 20 T. The reduction of the hyperfine magnetic field values can be related to the presence of the Cu atoms from the substrate that were dissolved in the bcc structure of Fe [62,65] during the electrodeposition process, therefore forming a solid solution of the Fe–Cu with bcc structure (Cu in the Fe matrix). The diamagnetism of the Cu reduces the hyperfine magnetic field in the body-centered cubic environment in which the atoms of the Fe are located. The paramagnetic singlet with an isomeric shift (δ) = 0.01 mm s^{-1} indicates the presence of Fe atoms in an fcc structure [65]. During the electrodeposition process, there is a diffusion of Fe atoms in the fcc structure of the Cu substrate, thus, forming a solid solution of the Cu–Fe with an fcc structure (Fe in the Cu matrix). Also, a second paramagnetic contribution, characterized by a doublet, is identified with the hyperfine parameters which are characteristic of Fe^{3+} cations in a paramagnetic environment of iron oxides that are formed during the electrodeposition process. However, these contributions are too low to modify material characteristics [60].

Table 2
Coercivity and normalized remanent magnetization of the Fe–Co coatings at different concentrations.

Sample	H_c/ Oe	(M_r/M_s)
Fe	72	0.14
$Fe_{87}Co_{13}$	645	0.18
$Fe_{64}Co_{36}$	811	0.13
$Fe_{44}Co_{56}$	86	0.31
$Fe_{25}Co_{75}$	27	0.34
Fe_7Co_{93}	262	0.18

Fig. 7 shows the Mössbauer spectra of $Fe_{87}Co_{13}$, $Fe_{64}Co_{36}$, $Fe_{44}Co_{56}$ and $Fe_{25}Co_{75}$ coatings fitted with two ferromagnetic sextets (blue and green lines) and a paramagnetic singlet (violet line), indicating the formation of a solid solution of the Cu–Fe as discussed above. The two sextets indicate that the Fe atoms are in two ferromagnetic sites with a similar chemical environment. The hyperfine magnetic field values between 36 T and 38 T are characteristic of Fe–Co magnetic alloys in different concentrations [65]. The presence of the Co atoms in the vicinity leads to an increase of the hyperfine field on the Fe atoms from the expected value of 33.3 T [65,66], hence confirming the formation of the Fe–Co alloy in these conditions. The $Fe_{25}Co_{75}$ coating showed two sextets with $B_{hf} = 32.9$ T (corresponding to the phase α–Fe, where there are only

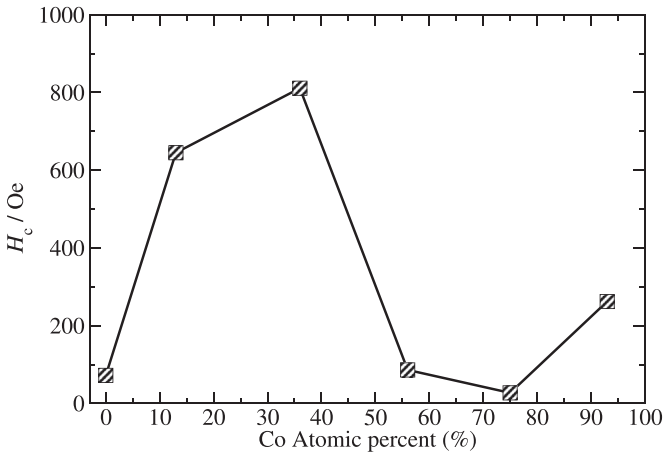

Fig. 5. Relationship between coercivity H_c and Co content in the Fe–Co film.

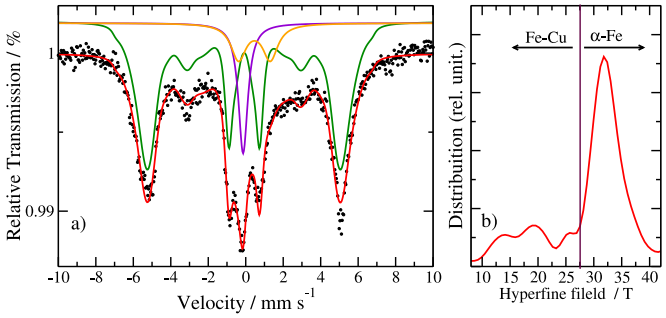

Fig. 6. Pure Fe coating: (a) Mössbauer spectra and (b) hyperfine field distribution.

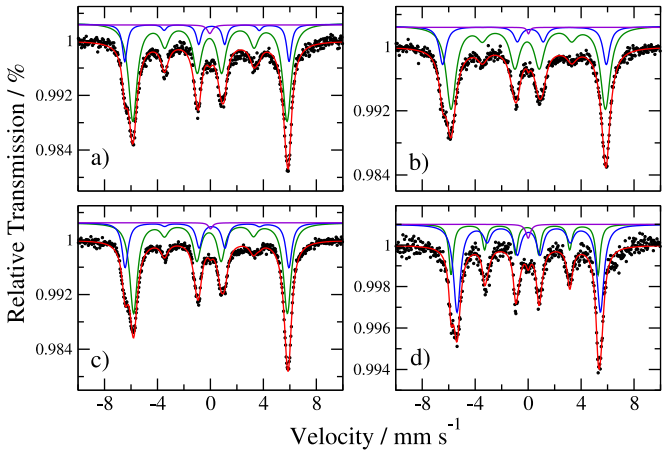

Fig. 7. Mössbauer spectra of (a) $Fe_{87}Co_{13}$, (b) $Fe_{64}Co_{36}$, (c) $Fe_{44}Co_{56}$ e (d) $Fe_{25}Co_{75}$ coatings.

Fe atoms in the vicinity [64]) and 34.8 T. This increase in the hyperfine field indicates that small amounts of the Co are in the vicinity of the Fe atoms, i.e. in the $Fe_{25}Co_{75}$ coating, resulting in the formation of an incomplete Fe–Co phase. Therefore, this behavior contributes to the magnetization results of the Co-rich coatings, where the coercive field values are reduced with the addition of the Co, indicating a reduction of the Fe–Co fraction in the coatings, and probably the formation of only one binary film. It is interesting to note that the fitted values of δ for the sub-spectra of $Fe_{87}Co_{13}$, $Fe_{64}Co_{36}$, $Fe_{44}Co_{56}$ were in the range 0.05 at 0.08 mm s^{-1} (with

Table 3
Parameters Mössbauer of Fe–Co coatings obtained from hyperfine adjustments.

Sample	Mössbauer parameters					
	Site	B_{hf}/ T	δ/ mm s^{-1}	Δ/ mm s^{-1}	$I_{2,5}$/ $I_{1,6}$	θ/ °
Fe	Distribution	8–42	0.02	0.01	0.05	15.6
	Doublet	–	0.56	1.70	–	–
	Singlet	–	0.01	–	–	–
$Fe_{84}Co_{13}$	Sextet 1	36.1	0.06	0.03	0.21	32.0
	Sextet 2	38.4	0.03	−0.36	0.15	26.7
	Singlet	–	0.07	–	–	–
$Fe_{64}Co_{36}$	Sextet 1	36.1	0.08	0.01	0.14	26.1
	Sextet 2	38.3	0.06	−0.43	0.006	5.1
	Singlet	–	0.12	–	–	–
$Fe_{44}Co_{56}$	Sextet 1	36.0	0.06	0.11	0.12	24.5
	Sextet 2	38.3	0.05	−0.38	0.06	17.4
	Singlet	–	0.11	–	–	–
$Fe_{25}Co_{75}$	Sextet 1	32.9	0.09	0.05	0.22	32.0
	Sextet 2	34.7	0.06	−0.12	0.40	42.8
	Singlet	–	0.10	–	–	–

respect to α–Fe). These values are compatible with values found by Kozlovskiy et al. [60] for electrodeposited Fe–Co alloys in the aqueous systems. Therefore, the found values of δ, and the B_{hf} values between 32 T and 38 T, confirm the formation of the Fe–Co alloy in the coatings without the presence of iron oxides.

The results of the Mössbauer study showed that the hyperfine magnetic field of the Fe nuclei increased with the addition of Co to the coatings. This arrangement of the Fe atoms in a bcc crystalline structure consists of eight equivalent atomic positions around each Fe atom, where each of the eight positions is occupied by the Fe atoms in the hyperfine magnetic field with the Fe nucleus 33 T. However, the substitution process of some Fe atoms by the Co atoms in the formation of the Fe–Co alloy leads to an increase in the values of the hyperfine magnetic field. This fact is related to the greater ferromagnetism of the Co, which is around the atoms of the Fe in the bcc structure, thus increasing the hyperfine magnetic field. In a similar study of the electrodeposited Fe–Co alloys in aqueous systems, Kozlovskiy et al. [60] showed that replacing an Fe atom with a Co atom increases the hyperfine magnetic field by approximately 0.9 T, indicating the formation of Fe–Co alloy. The incorporation of the Co atoms in the Fe bcc structure causes a minor distortion which is reflected by the values of a quadrupole shift (Δ) different to zero. This fact may be related to the characteristics of Co which has one additional electron than Fe.

An important characteristic observed in all samples analyzed by Mössbauer spectroscopy was an irregularity in the intensity of the absorption of lines two and five. This region of the spectrum carries information about the orientation of the magnetic moments [66]. Ferromagnetic materials produced in the form of very thin films have crystallographic and magnetic texture effects (preferential orientations), which can promote changes in the intensities of absorption in the Mössbauer lines. Through the Mössbauer spectroscopy, the magnetic texture of materials is determined from the relation of intensities of the six absorption lines from the ferromagnetic sextet. For materials that present a well-defined Mössbauer spectrum, the relation between the intensities and the angle θ formed between the incident gamma-ray beam and the orientation of the hyperfine magnetic field satisfies the following relations: $I_1 = 3$: $I_2 = 4\sin^2\theta / (1+\cos^2\theta)$: $I_3 = 1$: $I_4 = 1$: $I_5 = 4\sin^2\theta / (1+\cos^2\theta)$: $I_6 = 3$ [67]. In a situation in which the hyperfine magnetic field is parallel to the direction of the gamma-ray beam, that is $\theta = 0^\circ$, the relation between the relative intensities is 3:0:1:1:0:3. If the magnetization is perpendicular to the gamma-ray beam $\theta = 90^\circ$, one has a new configuration 3:4:1:1:4:3. Moreover, materials in the form of powders in which the magnetic orientations

are randomly distributed in relation to the beam of gamma-rays, the angular function $4\sin^2\theta$ / $(1+\cos^2\theta)$ has an average 2, resulting in a relation of relative intensities of 3:2:1:1:2:3 [67]. The reduction of lines 2 and 5 in all the coatings analyzed by Mössbauer spectroscopy shows that the materials duly studied have the magnetic texture with magnetic moments oriented in the direction of the propagation axis in the gamma-rays. The values of the angles formed between the magnetic moment vector and the gamma-ray beam in each analyzed coating are recorded in Table 3. The magnetic texture data are in agreement with the values found in the Fe–Co nanowires by Kozlovoskiy et al. [60], showing that our samples present a magnetic texture in the bulk film.

3.5. Electrocatalytic properties for HER

Fig. 8a shows the obtained polarization curves for the HER on Fe, $Fe_{87}Co_{13}$, $Fe_{64}Co_{36}$, $Fe_{44}Co_{56}$, $Fe_{25}Co_{75}$, Fe_7Co_{93}, and Co. It can be seen that HER overpotential increases with the increase of the Co content in the coating. Moreover, the performance of electrocatalyst materials can be evaluated considering the overpotential at a current density of 10 mA cm^{-2} [68]. These values are shown in Table 4. Therefore, a lower overpotential value of 89.2 mV for HER was observed for Fe electrocatalyst coatings, suggesting that among the investigated electrodeposited coatings, the Fe coatings are the best electrocatalysts for the HER.

In alkaline solutions, the HER process can occur in three steps. The reactions that describe these steps are represented by the following expressions [28,29,69–71].

$$M + H_2O + e^- \rightleftharpoons M - H_{ads} + OH^- \quad (2)$$

$$M - H_{ads} + H_2O + e^- \rightleftharpoons H_2 + M + OH^- \quad (3)$$

$$M - H_{ads} + M - H_{ads} \rightleftharpoons H_2 + 2M \quad (4)$$

In the first equation stage (Equation (2)), there is a hydrogen atom adsorption on the metallic surface (Volmer reaction). The second (Equation (3)) and, finally, the third (Equation (4)) stages may occur alternately, or simultaneously, depending on how the hydrogen atoms are adsorbed onto the catalytic surface, which may be by either electrochemical desorption (Heyrovsky reaction) or chemical desorption (Tafel reaction), respectively. Therefore, the process of producing H_2 in alkaline solutions is described by two reactions: Volmer-Heyrovsky or Volmer-Tafel. From the Tafel slope, it is possible to determine if the HER proceeds via either the Volmer, the Volmer-Heyrovsky, or the Volmer-Tafel mechanism, which are characterized by the Tafel slope ≈ -120 mV dec^{-1}, ≈ -40 mV dec^{-1} or ≈ -30 mV dec^{-1} at 298 K, respectively [28,68].

The calculation of the kinetic parameters for the HER Tafel slope (b) and exchange current (J_0) was carried out from a linear fit of the polarization curves by the Tafel equation (Equations (5) and (6)) [68], which are shown in Fig. 8b. In Equations (5) and (6), J_0 is the current exchange, η is the applied overpotential, a and b are the intercept and Tafel slope, respectively, and finally, J is the measured current density.

$$\eta = a + b \log J \quad (5)$$

$$J_0 = 10^{-a/b} \quad (6)$$

The calculated electrochemical kinetic parameters for the HER are listed in Table 4. For the Fe coatings, the calculated Tafel slope is 44.6 mV dec^{-1}, indicating that the HER on the Fe coating is controlled by the Volmer-Heyrovsky mechanism with the determining step being the Heyrovsky reaction. On the other hand, for the Co coating, the Tafel slope is 115.3 mV dec^{-1}, indicating that the Volmer reaction is the rate-determining step for the HER on the Co surface. For the Fe–Co coatings, all Tafel values were intermediate between those obtained for the Fe and the Co coatings, and they increased with increasing Co content. This particular fact

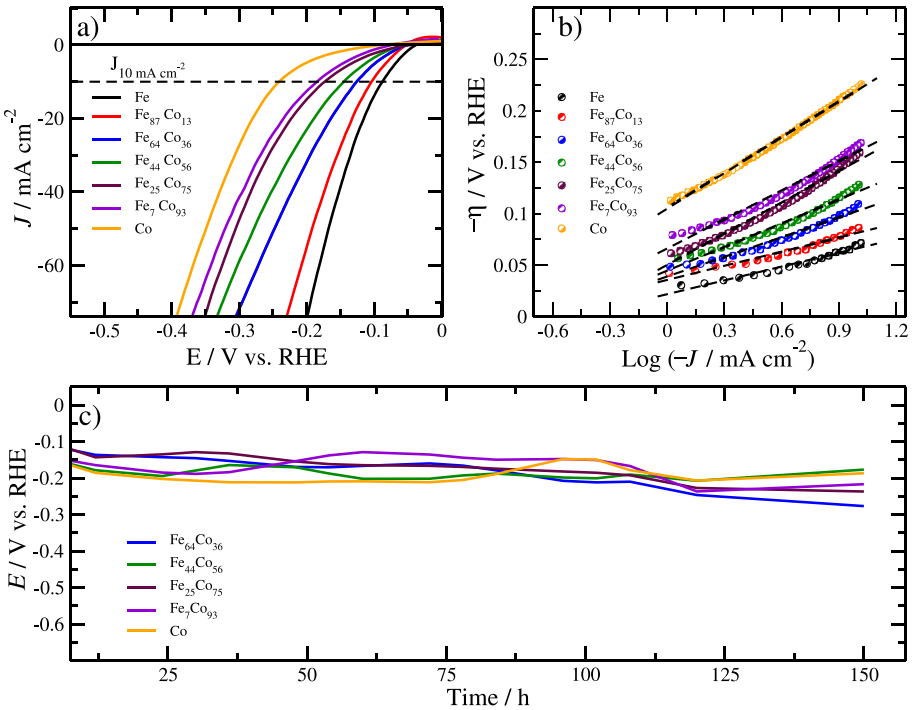

Fig. 8. (a) Polarization curves of Fe–Co catalysts, at a scan rate of 1 mV s^{-1} in 0.5 mol L^{-1} NaOH. (b) Tafel slope with linear fitting. (c) Stability test of the Fe–Co coatings in continuous operation for 150 h at 50 mA cm^{-2}.

Table 4
Electrochemical parameters for the HER in 0.5 mol L^{-1} NaOH at 298.15 K on Fe, Co, and Fe–Co coating obtained in different concentrations, and comparison with several catalysts in alkaline solution.

Catalyst	b/ mV dec^{-1}	J_0/ mA cm^{-2}	η (in 10 mA cm^{-2})/ mV	Reference
Fe	44.6	0.33	89.2	this work
$Fe_{87}Co_{13}$	45.8	0.28	104.2	this work
$Fe_{64}Co_{36}$	63.8	0.24	126.2	this work
$Fe_{44}Co_{56}$	76.7	0.26	145.5	this work
$Fe_{25}Co_{75}$	101.2	0.25	174.5	this work
Fe_7Co_{93}	98.2	0.20	186.6	this work
Co	115.3	0.11	243.2	this work
FeP	82	0.03	32	[17]
$Co_{0.59}Fe_{0.41}P$	72	0.57	92	[17]
CoP/CC	55	–	103	[74]
$Co_{0.5}Fe_{0.5}P$/CC	30	–	37	[74]
Fe_3C–NRs	46	–	49	[26]
FeNi–P	82	–	102	[75]
$CoFe_3O_4$/CC	91.4	–	254	[31]

demonstrates that both Fe and Co sites are active in the HER.

Previous investigations [72,73] have demonstrated that the hydrogen evolution activity is strongly correlated with the free energy of hydrogen to the electrocatalytic surface, where the free energy change for H* adsorption on the material surface can be obtained as a function of the total energy for the adsorption state, the energy of the pure surface, the energy of H^2 in the gas phase, and the entropy change of the process. Tang et al. [74] performed an extensive Density Function Theory (DFT) calculation which further revealed that Fe substitution of Co in CoFeP leads to a more optimal free energy of hydrogen adsorption on the catalyst surface. The calculations also revealed that the HER performances of the binary alloy $Fe_{0.5}Co_{0.5}P$ are similar to Pt-like activity, suggesting that the Fe sites are more electrocatalytic for the HER than the Co ones. In addition, the reduction of J_0 with the Co content in the coatings, shown in Table 4, indicates the highest contribution of Fe for HER of the coatings. Moreover, for comparison, Table 4 also displays the electrokinetic parameters for the HER on other electronic materials, which are published in the literature, demonstrating that our results are similar to those obtained by other authors.

To assess the stability of the Fe, Co, and Fe–Co coatings for a continuous test, the electrodeposited coatings were subjected to the tests for 150 h and the results are shown in Fig. 8c. During this process, it was observed that the Fe and Fe_{87} Co_{13} coatings did not present enough adherence to support the strong gas evolution during the stability test. Regarding the $Fe_{64}Co_{36}$, $Fe_{44}Co_{56}$, $Fe_{25}Co_{75}$, Fe_7Co_{93}, and Co coatings, a slight variation in the electrode potential was displayed by these coatings, while they had good mechanical stability and durability for the large-scale hydrogen production.

4. Conclusions

Fe–Co coatings were successfully electrodeposited on Cu surfaces from a eutectic mixture of choline chloride-urea, and no Fe or Co precipitates were observed after the electrodeposition. The electrodeposited Fe–Co coatings were characterized as soft magnetic materials. The Mössbauer study showed the formation of the Fe–Co intermetallic phase in the following electrodeposited coatings: $Fe_{87}Co_{13}$, $Fe_{64}Co_{36}$, $Fe_{44}Co_{56}$. Besides, a local magnetic texture along the growth axis of the Fe–Co coatings was also observed. The HER on Fe–Co coatings followed both the Volmer and Volmer-Heyrovsky mechanisms, indicating that both Fe and Co sites are active in the H^2 gas evolution, as well as the Fe–Co coatings being richer in Co, presenting good mechanical stability in long term tests of hydrogen evolution in the alkaline media. The Fe coating was the most suitable as electrocatalyst performance of HER. However, this coating did not present mechanical stability under strong gas evolution. The Fe–Co and Co coatings showed good mechanical stability under the strong gas evolution, except for the $Fe_{87}Co_{13}$ coating. Also, $Fe_{87}Co_{13}$, $Fe_{64}Co_{36}$, $Fe_{44}Co_{56}$ presented similar and even better siperior electrocatalytic performance in HER. Finally, Deep Eutectic Solvents are promising to be used as environmentally friendly electroplating solvents to produce electrodeposited Fe–Co coatings.

CRediT authorship contribution statement

Francisco G.S. Oliveira: Investigation, Conceptualization, Methodology, Writing - original draft. **F. Bohn:** Writing - original draft, Magnetic properties methodology. **Adriana N. Correia:** Project administration, Supervision. **Igor F. Vasconcelos:** Writing - review & editing, Supervision. **Pedro de Lima-Neto:** Project administration, Writing - review & editing, Supervision, Conceptualization, Methodology.

Declaration of competing interest

The authors declare that they have no known competing financial interests or personal relationships that could have appeared to influence the work reported in this paper.

Acknowledgements

This study was financed by the Brazilian funding agencies: Coordenação de Aperfeiçoamento de Pessoal de Nível Superior (CAPES), Conselho Nacional de Desenvolvimento Científico e Tecnológico (CNPq) and Fundação Cearense de Apoio ao Desenvolvimento Científico e Tecnológica (FUNCAP). The authors are would like to thank the Central Analítica UFC/ CT-INFRA/ MCTI-SISNANO/ Pró-Equipamentos CAPES for the support. Francisco G. S. Oliveira thanks FUNCAP and CAPES for his scholarship. Pedro de Lima-Neto and Adriana N. Correia thanks the financial support received from CNPq projects: 408626/2018-6, 304152/2018-8, 474832/2013-9, 400223/2014-7 and 305519/2015-8.

References

[1] Q. Dai, D. Berman, K. Virwani, J. Frommer, P.-O. Jubert, M. Lam, T. Topuria, W. Imaino, A. Nelson, Self–assembled ferrimagnet–polymer composites for magnetic recording media, Nano Lett. 10 (2010) 3216–3221, https://doi.org/10.1021/nl1022749.
[2] A. Masseboeuf, A. Marty, P. Bayle-Guillemaud, C. Gatel, E. Snoeck, Quantitative observation of magnetic flux distribution in new magnetic films for future high density recording media, Nano Lett. 9 (2009) 2803–2806, https://doi.org/

10.1021/nl900800q.
[3] Z. Quan, X. Zhang, W. Liu, X. Li, K. Addison, G.A. Gehring, X. Xu, Enhanced room temperature magnetoresistance and spin injection from metallic cobalt in Co/ZnO and Co/ZnAlO films, ACS Appl. Mater. Interfaces 5 (2013) 3607–3613, https://doi.org/10.1021/am303276b.
[4] F. Li, Y. Zhan, T.-H. Lee, X. Liu, A. Chikamatsu, T.-F. Guo, H.-J. Lin, J.C.A. Huang, M. Fahlman, Modified surface electronic and magnetic properties of $La_{0.6}Sr_{0.4}MnO_3$ thin films for spintronics applications, J. Phys. Chem. C 115 (2011) 16947–16953, https://doi.org/10.1021/jp112064y.
[5] D. Zhou, M. Zhou, M. Zhu, X. Yang, M. Yue, Electrodeposition and magnetic properties of FeCo alloy films, J. Appl. Phys. 111 (2012), https://doi.org/10.1063/1.3675063, 07A319.
[6] I. Shao, L. Romankiw, C. Bonhote, Stress in electrodeposited CoFe alloy films, J. Cryst. Growth 312 (2010) 1262–1266, https://doi.org/10.1016/j.jcrysgro.2009.11.061.
[7] K. Sundaram, V. Dhanasekaran, T. Mahalingam, Structural and magnetic properties of high magnetic moment electroplated conife thin films, Ionics 17 (2011) 835–842, https://doi.org/10.1007/s11581-011-0580-0.
[8] S. Mehrizi, M.H. Sohi, S.S. Ebrahimi, Study of microstructure and magnetic properties of electrodeposited nanocrystalline CoFeNiCu thin films, Surf. Coating. Technol. 205 (2011) 4757–4763, https://doi.org/10.1016/j.surfcoat.2011.03.070.
[9] N.N. Rozlin, A.M. Alfantazi, Nanocrystalline cobalt-iron alloy Synthesis and characterization, Mater. Sci. Eng., A 550 (2012) 388–394, https://doi.org/10.1016/j.msea.2012.04.092.
[10] S.F. Khaneghahi, S. Sharafi, Magnetic and structural properties of nano-structured $(Fe_{65}\ Co_{35})_{100-x}Cr_x$ (x=0, 10) powders prepared by mechanical alloying process, Adv. Powder Technol. 25 (2014) 211–218, https://doi.org/10.1016/j.apt.2013.04.001.
[11] Y. Wan, T. Cui, J. Xiao, G. Xiong, R. Guo, H. Luo, Engineering carbon fibers with dual coatings of FeCo and CuO towards enhanced microwave absorption properties, J. Alloys Compd. 687 (2016) 334–341, https://doi.org/10.1016/j.jallcom.2016.06.147.
[12] G. Reiss, A. Hütten, Applications beyond data storage, Nat. Mater. 4 (2005) 725–726, https://doi.org/10.1038/nmat1494.
[13] W.S. Seo, J.H. Lee, X. Sun, Y. Suzuki, D. Mann, Z. Liu, M. Terashima, P.C. Yang, M.V. McConnell, D.G. Nishimura, H. Dai, FeCo/graphitic-shell nanocrystals as advanced magnetic-resonance-imaging and near-infrared agents, Nat. Mater. 5 (2006) 971–976, https://doi.org/10.1038/nmat1775.
[14] Z. Wang, E. Feng, Q. Liu, J. Wang, D. Xue, Tuning stress-induced magnetic anisotropy and high frequency properties of FeCo films deposited on different curvature substrates, Phys. B Condens. Matter 407 (2012) 3872–3875, https://doi.org/10.1016/j.physb.2012.06.012.
[15] K. Seemann, H. Leiste, V. Bekker, A new generation of cmos-compatible high frequency micro-inductors with ferromagnetic cores: Theory, fabrication and characterisation, J. Magn. Magn Mater. 302 (2006) 321–326, https://doi.org/10.1016/j.jmmm.2005.05.042.
[16] A. Kozlovskiy, M. Zdorovets, K. Kadyrzhanov, I. Korolkov, V. Rusakov, L. Nikolaevich, O. Fesenko, O. Budnyk, D. Yakimchuk, A. Shumskaya, E. Kaniukov, FeCo nanotubes: possible tool for targeted delivery of drugs and proteins, Appl. Nanosci. 9 (2019) 1091–1099, https://doi.org/10.1007/s13204-018-0889-3.
[17] J. Hao, W. Yang, Z. Zhang, J. Tang, Metal organic frameworks derived $Co_x Fe_{1-x}P$ nanocubes for electrochemical hydrogen evolution, Nanoscale 7 (2015) 11055–11062, https://doi.org/10.1039/C5NR01955A.
[18] F. Golgovici, A. Pumnea, A. Petica, A.C. Manea, O. Brincoveanu, M. Enachescu, L. Anicai, Ni–Mo alloy nanostructures as cathodic materials for hydrogen evolution reaction during seawater electrolysis, Chem. Pap. 72 (2018), https://doi.org/10.1007/s11696-018-0486-7, 1889.
[19] S.A. Grigoriev, V.N. Fateev, Hydrogen Production by Water Electrolysis, John Wiley & Sons, Ltd, 2017, pp. 231–276. Ch. 6.
[20] M. Gong, D.-Y. Wang, C.-C. Chen, B.-J. Hwang, H. Dai, A mini review on nickel-based electrocatalysts for alkaline hydrogen evolution reaction, Nano Res. 9 (2016) 28–46, https://doi.org/10.1007/s12274-015-0965-x.
[21] F. Safizadeh, E. Ghali, G. Houlachi, Electrocatalysis developments for hydrogen evolution reaction in alkaline solutions - a Review, Int. J. Hydrogen Energy 40 (2015) 256–274, https://doi.org/10.1016/j.ijhydene.2014.10.109.
[22] L. Hostert, E.G.C. Neiva, A.J.G. Zarbin, E.S. Orth, Nanocatalysts for hydrogen production from borohydride hydrolysis graphene-derived thin films with Ag- and Ni-based nanoparticles, J. Mater. Chem. 6 (2018) 22226–22233, https://doi.org/10.1039/C8TA05834B.
[23] E.J. Popczun, J.R. McKone, C.G. Read, A.J. Biacchi, A.M. Wiltrout, N.S. Lewis, R.E. Schaak, Nanostructured nickel phosphide as an electrocatalyst for the hydrogen evolution reaction, J. Am. Chem. Soc. 135 (2013) 9267–9270, https://doi.org/10.1021/ja403440e.
[24] D. Voiry, H. Yamaguchi, J. Li, R. Silva, D.C.B. Alves, T. Fujita, M. Chen, T. Asefa, V.B. Shenoy, G. Eda, M. Chhowalla, Enhanced catalytic activity in strained chemically exfoliated WS2 nanosheets for hydrogen evolution, Nat. Mater. (2013) 850, https://doi.org/10.1038/nmat3700.
[25] W. Sides, N. Kassouf1, Q. Huang, Electrodeposition of ferromagnetic FeCo and FeCoMn alloy from choline chloride based deep eutectic solvent, J. Electrochem. Soc. 166 (2019) D77–D85, https://doi.org/10.1149/2.0181904jes.
[26] X. Fan, Z. Peng, R. Ye, H. Zhou, X. Guo, M3C (M: Fe, Co, Ni) nanocrystals encased in graphene nanoribbons: an active and stable bifunctional electrocatalyst for oxygen reduction and hydrogen evolution reactions, ACS Nano 9 (2015) 7407–7418, https://doi.org/10.1021/acsnano.5b02420.
[27] H. Fei, Y. Yang, Z. Peng, G. Ruan, Q. Zhong, L. Li, E.L.G. Samuel, J.M. Tour, Cobalt nanoparticles embedded in nitrogen-doped carbon for the hydrogen evolution reaction, ACS Appl. Mater. Interfaces 7 (2015) 8083–8087, https://doi.org/10.1021/acsami.5b00652.
[28] S. Wang, X. Zou, Y. Lu, S. Rao, X. Xie, Z. Pang, X. Lu, Q. Xu, Z. Zhou, Electrodeposition of nano-nickel in deep eutectic solvents for hydrogen evolution reaction in alkaline solution, Int. J. Hydrogen Energy 43 (2018) 15673–15686, https://doi.org/10.1016/j.ijhydene.2018.06.188.
[29] Y. Lu, S. Geng, S. Wang, S. Rao, Y. Huang, X. Zou, Y. Zhang, Q. Xu, X. Lu, Electrodeposition of NiMoCu coatings from roasted nickel matte in deep eutectic solvent for hydrogen evolution reaction, Int. J. Hydrogen Energy 44 (2019) 5704–5716, https://doi.org/10.1016/j.ijhydene.2019.01.072.
[30] P.N. Casciano, R.L. Benevides, R.A. Santana, A.N. Correia, P. de Lima-Neto, Factorial design in the electrodeposition of Co-Mo coatings and their evaluations for hydrogen evolution reaction, J. Alloys Compd. 723 (2017) 164–171, https://doi.org/10.1016/j.jallcom.2017.06.282.
[31] F. Yuan, X. Cheng, M. Wang, Y. Ni, Controlled synthesis of tubular ferrite MFe_2O_4 (M=Fe, Co, Ni) microstructures with efficiently electrocatalytic activity for water splitting, Electrochim. Acta 324 (2019), https://doi.org/10.1016/j.electacta.2019.134883, 134883.
[32] Y. Jing, H. Sohn, T. Kline, R.H. Victora, J.P. Wang, Experimental and theoretical investigation of cubic FeCo nanoparticles for magnetic hyperthermia, J. Appl. Phys. 105 (2009), https://doi.org/10.1063/1.3074136, 07B305.
[33] C. Wang, S. Peng, L.-M. Lacroix, S. Sun, Synthesis of high magnetic moment CoFe nanoparticles via interfacial diffusion in core/shell structured Co/Fe nanoparticles, Nano Research 2 (2009) 380–385, https://doi.org/10.1007/s12274-009-9037-4.
[34] P. Ong, S. Mahmood, T. Zhang, J. Lin, R. Ramanujan, P. Lee, R. Rawat, Synthesis of FeCo nanoparticles by pulsed laser deposition in a diffusion cloud chamber, Appl. Surf. Sci. 254 (2008) 1909–1914, https://doi.org/10.1016/j.apsusc.2007.07.186.
[35] W. Chang, C. Lin, H. Chang, C. Chiu, S. Chen, Magnetic property enhancement by sputtering magnetically soft films Co, Fe and Fe65Co35 on PrFeB-type permanent magnet ribbons, Surf. Coating. Technol. 200 (2006) 3366–3369, https://doi.org/10.1016/j.surfcoat.2005.07.053.
[36] W. Lu, M. Jia, M. Ling, Y. Xu, J. Shi, X. Fang, Y. Song, X. Li, Phase evolution and magnetic properties of FeCo films electrodeposited at different temperatures, J. Alloys Compd. 637 (2015) 552–556, https://doi.org/10.1016/j.jallcom.2015.03.036.
[37] D. Cao, X. Cheng, H. Feng, C. Jin, Z. Zhu, L. Pan, Z. Wang, J. Wang, Q. Liu, Investigation on the structure and dynamic magnetic properties of feco films with different thicknesses by vector network analyzer and electron spin resonance spectroscopy, J. Alloys Compd. 688 (2016) 917–922, https://doi.org/10.1016/j.jallcom.2016.07.110.
[38] L. Phua, N. Phuoc, C. Ong, Investigation of the microstructure, magnetic and microwave properties of electrodeposited Ni_xFe_{1-x}(x=0.2-0.76) films, J. Alloys Compd. 520 (2012) 132–139, https://doi.org/10.1016/j.jallcom.2011.12.164.
[39] S. Liao, High moment CoFe thin films by electrodeposition, IEEE Trans. Magn. 23 (1987) 2981–2983, https://doi.org/10.1109/tmag.1987.1065555.
[40] X. Liu, P. Evans, G. Zangari, Electrodeposited Co-Fe and Co-Fe-Ni alloy films for magnetic recording write heads, IEEE Trans. Magn. 36 (2000) 3479–3481, https://doi.org/10.1109/20.908866.
[41] J. Vijayakumar, S. Mohan, S.A. Kumar, S. Suseendiran, S. Pavithra, Electrodeposition of Ni-Co-Sn alloy from choline chloride-based deep eutectic solvent and characterization as cathode for hydrogen evolution in alkaline solution, Int. J. Hydrogen Energy 38 (2013) 10208–10214, https://doi.org/10.1016/j.ijhydene.2013.06.068.
[42] F.A. Lowenheim, Electroplating, McGraw-Hill Companies, 1978.
[43] X. Liu, G. Zangari, L. Shen, Electrodeposition of soft, high moment Co-Fe-Ni thin films, J. Appl. Phys. 87 (2000) 5410–5412, https://doi.org/10.1063/1.373359.
[44] A.P. Abbott, G. Capper, K.J. McKenzie, K.S. Ryder, Electrodeposition of zinc-tin alloys from deep eutectic solvents based on choline chloride, Special Issue In Honour of David Schiffrin 599 (2007) 288–294, https://doi.org/10.1016/j.jelechem.2006.04.024.
[45] A.P. Abbott, G. Capper, D.L. Davies, R.K. Rasheed, V. Tambyrajah, Novel solvent properties of choline chloride/urea mixtures, Chem. Commun. 599 (2003) 70–71, https://doi.org/10.1039/B210714G.
[46] A.P. Abbott, D. Boothby, G. Capper, D.L. Davies, R.K. Rasheed, Deep eutectic solvents formed between choline chloride and carboxylic acids versatile alternatives to ionic liquids, J. Am. Chem. Soc. 126 (2004) 9142–9147, https://doi.org/10.1021/ja048266j.
[47] Q. Zhang, K. De Oliveira Vigier, S. Royer, F. Jérôme, Deep eutectic solvents: syntheses, properties and applications, Chem. Soc. Rev. 41 (2012) 7108–7146, https://doi.org/10.1039/C2CS35178A.
[48] A. Paiva, R. Craveiro, I. Aroso, M. Martins, R.L. Reis, A.R.C. Duarte, Natural deep eutectic solvents - solvents for the 21st century, ACS Sustain. Chem. Eng. 2 (2014) 1063–1071, https://doi.org/10.1021/sc500096j.
[49] M. Li, Z. Wang, R.G. Reddy, Cobalt electrodeposition using urea and choline chloride, Electrdoi :chimica Acta 123 (2014) 325–331, https://doi.org/10.1016/j.electacta.2014.01.052.
[50] T. Yanai, K. Shiraishi, Y. Watanabe, T. Ohgai, M. Nakano, K. Suzuki, H. Fukunaga, Magnetic Fe-Co films electroplated in a deep-eutectic-solvent-

based plating bath, J. Appl. Phys. 117 (2015) 17A925, https://doi.org/10.1063/1.4918782.
[51] Q.B. Zhang, Y.X. Hua, Electrochemical synthesis of copper nanoparticles using cuprous oxide as a precursor in choline chloride-urea deep eutectic solvent: nucleation and growth mechanism, Phys. Chem. Chem. Phys. 16 (2014) 27088–27095, https://doi.org/10.1039/C4CP03041A.
[52] A.P. Abbott, K. El Ttaib, G. Frisch, K.J. McKenzie, K.S. Ryder, Electrodeposition of copper composites from deep eutectic solvents based on choline chloride, Phys. Chem. Chem. Phys. 11 (2009) 4269–4277, https://doi.org/10.1039/B817881J.
[53] P. Lammel, L.D. Rafailovic, M. Kolb, K. Pohl, A.H. Whitehead, G. Grundmeier, B. Gollas, Analysis of rain erosion resistance of electroplated nickel-tungsten alloy coatings, Surf. Coating. Technol. 206 (2012) 2545–2551, https://doi.org/10.1016/j.surfcoat.2011.11.009.
[54] N. Eliaz, T. Sridhar, E. Gileadi, Sdoi :nthesis and characterization of nickel tungsten alloys by electrodeposition, Electrochim. Acta 50 (2005) 2893–2904, https://doi.org/10.1016/j.electacta.2004.11.038.
[55] M. Obradović, R. Stevanović, A. Despić, Electrochemical deposition of Ni-W alloys from ammonia-citrate electrolyte, J. Electroanal. Chem. 552 (2003) 185–196, https://doi.org/10.1016/S0022-0728(03)00151-7.
[56] Z. Ghaferi, K. Raeissi, M. Golozar, H. Edris, Characterization of nanocrystalline Co-W coatings on Cu substrate, electrodeposited from a citrate-ammonia bath, Surf. Coating. Technol. 206 (2011) 497–505, https://doi.org/10.1016/j.surfcoat.2011.07.074.
[57] I. Shao, L. Romankiw, C. Bonhote, Stress in electrodeposited cofe alloy films, J. Cryst. Growth 312 (2010) 1262–1266, https://doi.org/10.1016/j.jcrysgro.2009.11.061.
[58] A. Sakita, E. Passamani, H. Kumar, D. Cornejo, C. Fugivara, R. Noce, A. Benedetti, Influence of current density on crystalline structure and magnetic properties of electrodeposited Co-rich CoNiW alloys, Mater. Chem. Phys. 141 (2013) 576–581, https://doi.org/10.1016/j.matchemphys.2013.05.066.
[59] Y. Song, W. Lu, Y. Xu, J. Shi, X. Fang, Growth of single-crystalline Co7Fe3 nanowires via electrochemical deposition and their magnetic properties, J. Alloys Compd. 652 (2015) 179–184, https://doi.org/10.1016/j.jallcom.2015.08.206.
[60] A. Kozlovskiy, A. Zhanbotin, M. Zdorovets, I. Manakova, A. Ozernoy, T. Kiseleva, K. Kadyrzhanov, V. Rusakov, E. Kanyukov, Mössbauer research of Fe/Co nanotubes based on track membranes, Nucl. Instrum. Methods Phys. Res. Sect. B Beam Interact. Mater. Atoms 381 (2016) 103–109, https://doi.org/10.1016/j.nimb.2016.05.026.
[61] S.S. Maklakov, S.A. Maklakov, I.A. Ryzhikov, V.A. Amelichev, K.V. Pokholok, A.N. Lagarkov, Mössbauer study of disordering in thin sputtered FeCo-SiO_2 and FeCo films, J. Alloys Compd. 536 (2012) 33–37, https://doi.org/10.1016/j.jallcom.2012.05.022.
[62] P. Crespo, N. Menéndez, J. Tornero, M. Barro, J. Barandiarán, A.G. Escorial, A. Hernando, Mössbauer spectroscopy evidence of a spinodal mechanism for the thermal decomposition of f.c.c. FeCu, Acta Mater. 46 (1998) 4161–4166, https://doi.org/10.1016/S1359-6454(98)00111-6.
[63] S.B. Dalavi, M.M. Raja, R.N. Panda, FTIR, magnetic and Mössbauer investigations of nano-crystalline Fe_xCo_{1-x} (0.4 ≥x 0≤.8) alloys synthesized via a superhydride reduction route, New J. Chem. 39 (2015) 9641–9649, https://doi.org/10.1039/C5NJ01727K.
[64] M.F. Casula, G. Concas, F. Congiu, A. Corrias, A. Falqui, G. Spano, Near equiatomic FeCo nanocrystalline alloy embedded in an alumina aerogel matrix: microstructural features and related magnetic properties, J. Phys. Chem. B 109 (2005) 23888–23895, https://doi.org/10.1021/jp0546554.
[65] J. Williams, H. Blythe, V. Fedosyuk, An investigation of electrodeposited granular CuFe alloyed films, J. Magn. Magn Mater. 155 (1996) 355–357, https://doi.org/10.1016/0304-8853(95)00693-1.
[66] K.V. Frolov, D.L. Zagorskii, I.S. Lyubutin, M.A. Chuev, I.V. Perunov, S.A. Bedin, A.A. Lomov, V.V. Artemov, S.N. Sulyanov, Magnetic and structural properties of Fe–Co nanowires fabricated by matrix synthesis in the pores of track membranes, JETP Lett. (Engl. Transl.) 105 (2017) 319–326, https://doi.org/10.1134/S0021364017050083.
[67] F.J.B. Dominic, P.E. Dickson, Mössbauer Spectroscopy, Cambridge University Press, 1986.
[68] J. Wang, F. Xu, H. Jin, Y. Chen, Y. Wang, Non-noble metal-based carbon composites in hydrogen evolution reaction: fundamentals to applications, Adv. Mater. 29 (2017) 1605838, https://doi.org/10.1002/adma.201605838.
[69] J. Huot, L. Brossard, Time dependence of the hydrogen discharge at 70 C on nickel cathodes, Int. J. Hydrogen Energy 12 (1987) 821–830, https://doi.org/10.1016/0360-3199(87)90103-0.
[70] Y. Choquette, L. Brossard, H. Ménard, Leaching of raney nickel composite-coated electrodes, J. Appl. Electrochem. 20 (1990) 855–863, https://doi.org/10.1007/BF01094317.
[71] N. Krstajić, M. Popović, B. Grgur, M. Vojnović, D. Śepa, On the kinetics of the hydrogen evolution reaction on nickel in alkaline solution: Part i. the mechanism, J. Electroanal. Chem. 512 (2001) 16–26, https://doi.org/10.1016/S0022-0728(01)00590-3.
[72] Y. Zheng, Y. Jiao, M. Jaroniec, S.Z. Qiao, Advancing the electrochemistry of the hydrogen-evolution reaction through combining experiment and theory, Angew. Chem. Int. Ed. 54 (2015) 52–65, https://doi.org/10.1002/anie.201407031.
[73] M. Cabán-Acevedo, M.L. Stone, J.R. Schmidt, J.G. Thomas, Q. Ding, H.-C. Chang, M.-L. Tsai, J.-H. He, S. Jin, Efficient hydrogen evolution catalysis using ternary pyrite type cobalt phosphosulphide, Nat. Mater. 14 (2015) 1245–1251, https://doi.org/10.1038/nmat4410.
[74] C. Tang, L. Gan, L.W. Zhang, Rong, X. Jiang, A.M. Asiri, X. Sun, J. Wang, L. Chen, Ternary Fe_xCo^{1-x} P nanowire array as a robust hydrogen evolution reaction electrocatalyst with Pt-like activity: experimental and theoretical insight, Nano Lett. 16 (2016) 6617–6621, https://doi.org/10.1021/acs.nanolett.6b03332.
[75] Q. Yan, T. Wei, J. Wu, X. Yang, M. Zhu, K. Cheng, K. Ye, K. Zhu, J. Yan, D. Cao, G. Wang, Y. Pan, Self-supported FeNi-P nanosheets with thin amorphous layers for efficient electrocatalytic water splitting, ACS Sustain. Chem. Eng. 6 (2018) 9640–9648, https://doi.org/10.1021/acssuschemeng.7b04743.